International Journal of Nanoelectronics and Materials
Volume 16, No. 3, July 2023 [607-620]

Investigation of the Electrical Characteristics of AlGaN/AlN/GaN Heterostructure MOS-HEMTs with TiO_2 High-*k* Gate Insulator

Driss Bouguenna[1,3*], Abbès Beloufa[2,3], Khaled Hebali[1,4], Sajad Ahmad Loan[5]

[1] Laboratory of Geomatics, Ecology and Environment, Faculty of Nature and Life Sciences, University Mustapha Stambouli of Mascara, Mascara 29000, Algeria
[2] Laboratory of Applied Materials, Centre de Recherches (ex-CFTE), University of Sidi Bel Abbès, Sidi Bel Abbès 22000, Algeria
[3] Department of Science and Technology, Faculty of Science and Technology, University Mustapha Stambouli of Mascara, Mascara 29000, Algeria
[4] Department of Physics, Faculty of Exact Science, University Mustapha Stambouli of Mascara, Mascara 29000, Algeria
[5] Department of Electronics and Communication Engineering, Jamia Millia Islamia, New Delhi 110025, India

Received 10 August 2022, Revised 9 October 2022, Accepted 26 October 2022

ABSTRACT

This paper investigates the impact of TiO_2 high-k gate insulator on the electrical characteristics of AlGaN/AlN/GaN MOS-HEMT transistors using MATLAB and Atlas-TCAD simulation software. The physical analytical model of the MOS-HEMTs is used for simulation from Al_2O_3, HfO_2, and TiO_2 as the gate dielectric materials, which provide higher performance and reliability of the MOS-HEMT devices. The device shows a good improvement in its result of the DC and AC characteristics with different permittivity of insulator materials. Thus, the DC and AC performance of GaN MOS-HEMTs is higher than with other insulators, such as Al_2O_3 and HfO_2 by using TiO_2 as the gate dielectric. Moreover, the simulation results proved that TiO_2 is the better gate dielectric material to enhance the electrical reliability of the power switching devices for high-temperature applications such as electric automobiles.

Keywords: AlGaN/AlN/GaN, MOS-HEMTs, high-*k*, DC and AC performance, Atlas-TCAD

1. INTRODUCTION

Recently, many subjects of intense research have emerged as attractive candidates to investigate in future high-power microwave and low noise applications, such as AlGaN/GaN heterostructures based metal-insulator/oxide-semiconductor high electron mobility transistors (MIS/MOS-HEMTs), thanks to their superior material physical and electrical properties [1-4]. However, the conventional AlGaN/GaN HEMTs are largely impaired by high gate leakage current, which limits the gate voltage swing, and therefore the maximum current of the channel could, therefore reach [5, 6] by using widely high-*k* insulator materials, including Al_2O_3 [7-9], HfO_2 [10], and TiO_2 [11-15] which have been employed as gate insulator (oxide) dielectric and surface passivation materials to improve the electrical device performance of GaN HEMTs [1].

Moreover, the binary oxide materials are thermodynamically stable when they are contacted with III-V semiconductors. Among the high-*k* dielectric insulator materials, Al_2O_3, HfO_2, and TiO_2 are promising as gate insulator materials in III-V semiconductor materials based device, thanks to the wide bandgap materials (8.8, 5.8, and 3.5) eV and moderate permittivity (9, 25, and 80) of Al_2O_3, HfO_2, and TiO_2, respectively [10, 16].

Besides, Smorchkova *et al* [17] proposed that the insertion of a very thin AlN binary transition layer between the AlGaN barrier layer and the GaN buffer layer increases the concentrations of

* Corresponding author: bouguenna.driss@univ-mascara.dz

2-DEG formed at the AlGaN/GaN heterointerface, reduces the alloy scattering of 2DEG, improves electron mobility, and provides better carrier confinement owing to the large band offset and the effective polarization induced charge at the heterointerface AlN/GaN [2, 4, 8].
Moreover, 1 nm of the optimal AlN transition layer thickness is required for high electron mobility [18].

The problem in the electrical properties includes the bulk, the surface, and the interface trap states in the semiconductor material, the gate leakage, and the large transconductance dispersion of GaN HEMTs. There are still hurdles in the research. MOS-HEMTs based on AlGaN/GaN heterostructure exhibited good static and dynamic performance [2]. The vital factor influencing the device's operation is the oxide or insulator material type so as to achieve better performance.

Besides, Amarnath *et al.* [19] have presented their work on static and dynamic with different gate lengths of AlGaN/AlN/GaN heterostructure based MOS-HEMTs. However, the impact of the gate insulator type is not considered in their work.

Furthermore, the important parameter is the gate insulator material type to solve the distortion performance in the case of MOS-HEMTs. It has been reported in other literature [9-15]. However, the impact of TiO_2 gate insulator type and thickness on the static (DC) and dynamic (AC) electrical performance of AlGaN/GaN MOS-HEMTs has not been taken into consideration yet.

This paper tackles the effect of TiO_2 gate dielectric material on the DC and AC characteristics of GaN-based MOS-HEMTs by using a simulation study and comparing the results with other gate dielectric materials such as Al_2O_3 and HfO_2.

Moreover, the rest of the paper is organized as follows: the section on the physical model formulations derives the analytical expressions of the sheet carrier density, the I-V, C-V and the cut-off and maximum oscillation frequencies. In the results and discussions section, the numerical simulation results of the analytical model obtained by MATLAB for the DC and AC electrical performance of GaN MOS-HEMTs are presented and calibrated with necessary results extracted by Atlas-TCAD simulator software [20]. The experimental data from the available literature have proved the validity of the proposed model. Finally, the conclusion is drawn in section 4.

2. PHYSICAL MODEL FORMULATIONS

A schematic cross-sectional view of the AlGaN/GaN conventional HEMTs and MOS-HEMTs structures is shown in Fig. 1, where d_{ox} is the insulator oxide layer thickness, d_{AlGaN} represents barrier layer thickness, d_{AlN} is the transition layer thickness, and d_{GaN} is the buffer layer thickness. The gate insulator materials, such as Al_2O_3, HfO_2, and TiO_2 have been used in the simulation study. Besides, the dimensions and materials have been considered in the simulation.

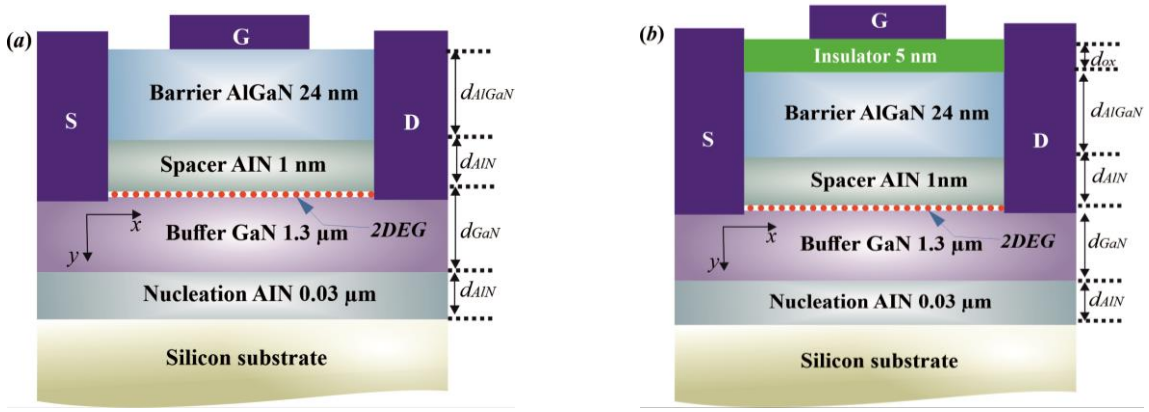

Fig. 1. Cross-sectional schematic of (a) conventional HEMTs and (b) MOS-HEMTs on AlGaN/AlN/GaN heterostructure.

2.1 Gate Leakage Current Model

The gate leakage current, especially in high-power switching device applications leads to high off-state power consumption. The gate leakage current mechanisms in insulator/AlGaN/AlN/GaN heterostructure are analyzed by the temperature-dependent Poole-Frenkel emission model. The gate leakage current variation related to the Poole-Frenkel emission can be expressed by [21]

$$I_g = C_{PF} A E_{ox} exp\left[-\frac{q\left(Q_f-(qE_{ox}/\pi\varepsilon_{ox})\right)}{k_B T}\right]. \quad (1)$$

Where C_{PF} represents the Poole-Frenkel constant, A is the gate contact area and E_{ox} is the electric field across the insulator layer, q is the electronic charge, Q_f is the interface state density, and ε_{ox} is the insulator layer permittivity. k_B and T are the Boltzmann's constant and the temperature, respectively.

2.2 Sheet Carrier Density Model

The 2-DEG is formed in the AlN/GaN quasi-triangular quantum well. Among the principal factors controlling the electrical device operation and heterostructure performance, it can be obtained by self-consistent solution of the Poisson's and Schrödinger's equations, which have been reported by K. Jena *et al.* [21, 22].

The analytical expression for sheet carrier concentration n_s can be formulated as [23]

$$n_s = \frac{C_g}{q}\left[V_{g0}\frac{V_{g0}-\theta(V_{g0})^{2/3}}{V_{g0}+2\theta(V_{g0})^{2/3}}\right] \quad (2)$$

Where $\theta = (\gamma_0/3)(C_g/q)^{2/3}$ and γ_0 represents the fitting parameter extracted from data enlisted in Table 2, C_g represents the total gate capacitance. $V_{g0} = V_g - V_{off} - V_x$, V_g is the gate voltage, V_{off} represents the pinch-off voltage, and V_x represents the channel potential at point x.

The total gate capacitance C_g of the GaN MOS-HEMTs device can be determined by the smallest capacitance component among the three capacitances C_{ox}, C_{AlGaN}, and C_{AlN} series-connected is shown in Fig. 2(a).

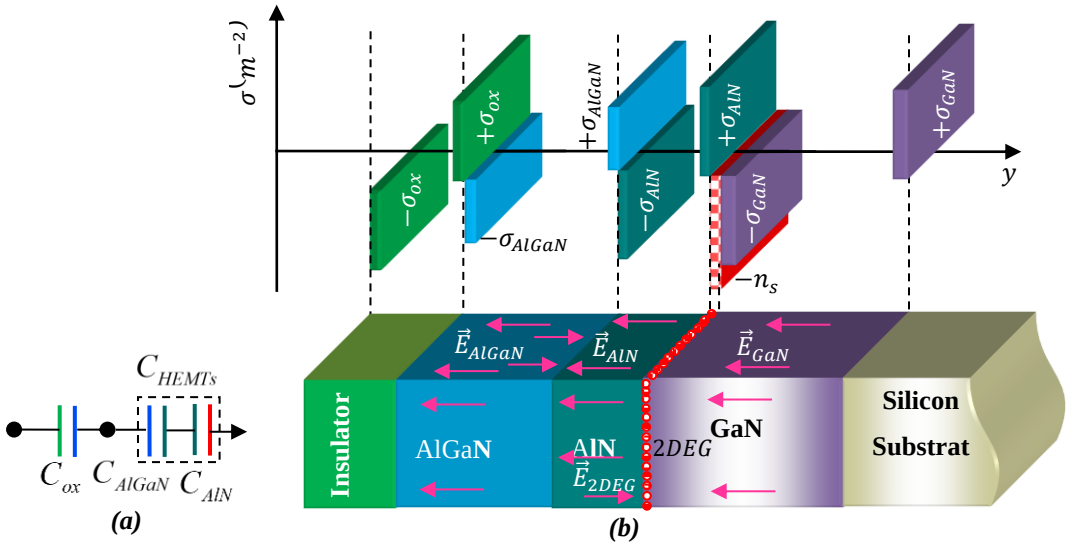

Fig. 2. (a) Equivalent circuit diagram for gate capacitance in AlGaN/GaN MOS-HEMTs and (b) charge distribution profile of an insulator/AlGaN/AlN/GaN heterostructure.

The gate capacitance C_g of GaN MOS-HEMTs, it can be expressed as follows

$$\frac{1}{C_g} = \frac{1}{C_{ox}} + \frac{1}{C_{HEMTs}} \tag{3}$$

The equivalent capacitance C_{HEMTs} of GaN HEMTs, it can be calculated as [24]

$$\frac{1}{C_{HEMTs}} = \frac{1}{C_{AlGaN}} + \frac{1}{C_{AlN}} \tag{3a}$$

$$C_g = \frac{C_{ox} \times C_{AlGaN} \times C_{AlN}}{C_{ox} \times C_{AlGaN} + C_{ox} \times C_{AlN} + C_{AlGaN} \times C_{AlN}} \tag{3b}$$

Where $C_{ox} = \varepsilon_0 \varepsilon_{ox} / d_{ox}$ represents the insulator capacitance layer and d_{ox} is the insulator layer thickness, $C_{AlGaN} = \varepsilon_0 \varepsilon_{AlGaN} / d_{AlGaN}$ and d_{AlGaN} are represent the capacitance and the barrier layer thickness of AlGaN, respectively. $C_{AlN} = \varepsilon_0 \varepsilon_{AlN} / d_{AlN}$ and d_{AlN} are represent the capacitance and the transition layer thickness of AlN.

The charge distribution profile of an insulator/AlGaN/AlN/GaN heterostructure is shown in Fig. 2(b). The surface and interface charge can be observed as four pairs of infinite charged planes with an equal quantity of heterogeneous charges.

2.3 Drain Current Model

The drain current I_{ds} model can be expressed as [23]

$$I_{ds} = \frac{\mu_0 W_g C_g}{L_g \rho} \left[\sum_{i=1}^{6} k_i \left(\psi_{gd}^i - \psi_{gs}^i \right) + k_0 ln \frac{\psi_{gd}}{\psi_{gs}} \right]. \tag{4}$$

Where $\psi_{gs} = \left(V_{gs} - V_{th}\right)^{1/3} + 2\theta$, $\psi_{gd} = \left(V_{gs} - V_{th} - V_{ds}\right)^{1/3} + 2\theta$, $\rho = 1 - \left[(V_{ds} - V_s)/E_T L_g\right]$, E_T represents the critical electric field, with a limit at $V(x = 0) = V_s = 0\ V$ and $V\left(x = L_g\right) = V_d = V_{ds}$.

The expressions for constant terms $k_i (i = 1, \ldots, 6)$ obtained during the integration of Eq. (4) are given in Table I.

Table 1 Expressions for constant terms $k_i (i = 1, \ldots, 6)$ obtained during the integration [23].

Constants	Expressions
k_0	$-288\theta^6$
k_1	$272\theta^5$
k_2	$-960\theta^4$
k_3	$200\theta^3$
k_4	$-70\theta^2$
k_5	39θ
k_6	-3

2.4 Transconductance Model

Among the important electrical parameters for evaluating the DC electrical performance is the intrinsic transconductance g_m of HEMTs device which plays a significant role, and is defined as follows:

$$g_m = \left.\frac{\partial I_{ds}}{\partial V_{gs}}\right|_{V_{ds}=const}. \tag{5}$$

Once a drain-source current model is developed, obtaining the transconductance numerically from the calculated current is a common practice. However, dedicated physical analytical expressions for the transconductance are developed in [25].

In the linear region, the transconductance can be obtained by differentiating Eq. (4) w.r.t. gate voltage V_{gs}, is given as [26]

$$g_m = -\frac{\mu_0 W_g C_g}{L_g \rho}\left[\frac{1}{3\left(\psi_{gd}-2\theta\right)^2 - 3\left(\psi_{gs}-2\theta\right)^2}\Omega_1\right]. \tag{6}$$

$$\text{Where } \Omega_1 = \begin{bmatrix} \frac{288\theta^6}{(\psi_{gd}-\psi_{gs})} + 272\theta^5 + 1920\theta^4\left(\psi_{gd}-\psi_{gs}\right) + 600\theta^3\left(\psi_{gd}-\psi_{gs}\right)^2 \\ -280\theta^2\left(\psi_{gd}-\psi_{gs}\right)^3 + 195\theta\left(\psi_{gd}-\psi_{gs}\right)^4 - 18\left(\psi_{gd}-\psi_{gs}\right)^5 \end{bmatrix}. \tag{6a}$$

2.5 Capacitances Model

The gate-to-source capacitance C_{gs} and gate-to-drain capacitance C_{gd} models can be expressed as, respectively [26]

$$C_{gs} = \frac{\mu_0 (qW_g\rho)^2}{I_{ds}} \left[\left(V_{gs} - V_{th} - V_{ds}\right)^{1/3} - \left(V_{gs} - V_{th}\right)^{1/3} \right] \left(\frac{g_m}{I_{ds}} - 1\right) - \frac{qW\rho}{E_T} V_{\mathrm{ds}} - \frac{L_g g_m}{\mu_0 E_T} \quad (7)$$

$$C_{gd} = \frac{\mu_0 (qW_g\rho)^2}{I_{ds}} \left[\left(V_{gs} - V_{th} - V_{\mathrm{ds}}\right)^{1/3} - \left(V_{\mathrm{gs}} - V_{th}\right)^{1/3} \right] \left(\frac{g_d}{I_{ds}} - 1\right) - \frac{qW\rho}{E_T} \left(V_{gs} - V_{th} - V_{ds}\right) - \frac{L_g g_d}{\mu_0 E_T} \quad (8)$$

2.5 Cut-off Frequency Model

The cut-off frequency f_T is one the primary for analyzing the device electrical performance at high-frequency regime, determines that the optimal switching speed of the device, which can be obtained as [26, 27]

$$f_T = \frac{g_m}{2\pi\left(C_{gs}+C_{gd}\right)} \quad (9)$$

2.6 Power Gain Maximum Oscillation Frequency Model

The power gain maximum oscillation frequency f_{max} can be expressed as [28]

$$f_{max} = \frac{f_T}{\sqrt{4R_g\left(g_d + 2\pi f_T C_{gd}\right)}}. \quad (10)$$

Where R_g is the gate resistance and g_d represents the output conductance.

Table 2 gives the analytical model parameters used in numerical simulations.

Table 2 List of model parameters used in numerical simulation.

Parameters	Description	Value	Unit	Refs.
E_T	Critical electric field	178×10^5	V/m	[29]
R_g	Gate resistance	86.7	Ω	[8]
ε_0	Vacuum permittivity	8.854×10^{-12}	F/m	[9]
ε_{AlN}	Spacer layer permittivity	$10.3\varepsilon_0$	F/m	[19]
$\sigma_{AlN/GaN}$	Polarization	6.5×10^{17}	m^{-2}	[26]
$\Delta E_C^{AlN/GaN}$	Conduction band offset	1.7	eV	[28]
μ_0	Low field mobility	0.06	m^2/Vs	[9]
γ_0	Fitting parameter	4×10^{-12}	$Vcm^{4/3}$	[24]

3. RESULTS AND DISCUSSIONS

In this section, the DC and AC electrical characteristics of GaN MOS-HEMTs with different gate insulator materials such as Al_2O_3, HfO_2 and TiO_2 are discussed and compared with experimental data extracted from [8]. The analytical model parameters of AlGaN/GaN MOS-HEMT devices used for numerical simulations of the DC and AC characteristics of three devices are indicated in Table 3.

Table 3 Model parameters of three devices details used for numerical simulations.

Parameters	Description	Al_2O_3	HfO_2	TiO_2
$Q_f\ (m^{-2})$	Fixed charge density	$5x10^{17}$[26]	$3x10^{16}$ [26]	$7x10^{16}$ [15]
$\varepsilon_{ox}(F/m)$	Insulator permittivity	$10\varepsilon_0$ [25]	$25\varepsilon_0$ [10]	$80\varepsilon_0$ [13, 14]
$E_g(eV)$ (300 K)	Gap energy	8.9 [25]	5.8 [30]	3.5 [16]
$\chi_{ox}\ (eV)$	Insulator electron affinity	1.35 [31]	2 [32]	2.95 [33]
$\Delta E_C^{ox/AlGaN}(eV)$	Conduction band offset	1.8 [34]	1.1 [34]	-1.1 [35]
$V_{th}\ (V)$	Threshold voltage	-5.4 [8]	-5.4 [36]	-5.4 [12]
$d_{ox}(nm)$	Insulator thickness	5 [36, 38]	5 [39]	5 [40]
$d_{AlGaN}\ (nm)$	Barrier thickness	24 [8]	24 [41]	24 [8]
$x(\%)$	Aluminum mole fraction	30 [8]	30 [10]	25~30 [8, 13]
$d_{AlN}(nm)$	Transition thickness	1 [8]	1 [30]	1 [42]
$d_{GaN}(\mu m)$	Buffer thickness	1.3 [8]	1.3 ---	1.3 ---
$L_g\ (\mu m)$	Gate length	1.2 [8]	1.2 ---	1.2 ---
$W_g\ (\mu m)$	Gate width	100 [26]	100 [26]	100 [8]

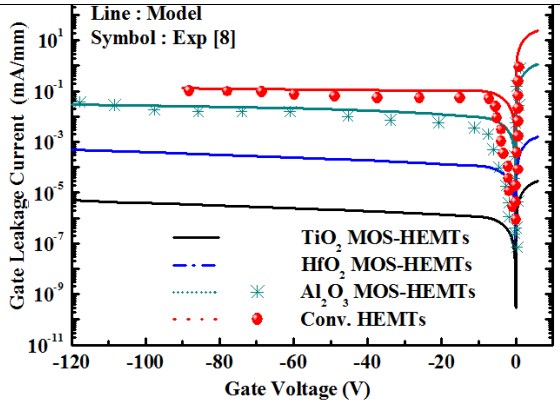

Fig. 3. Simulation results of the gate leakage current of the conventional HEMTs and MOS-HEMTs in comparison with experimental data.

The simulation results of the gate leakage current characteristics of conventional HEMTs and MOS-HEMTs with different gate dielectrics such as Al_2O_3, HfO_2, and TiO_2 in comparison with experimental data are shown in Fig. 3. In reverse bias, the gate leakage current can be suppressed by more than five and four orders of magnitude in the case of TiO_2-based MOS-HEMTs is observed to be lower than that of conventional HEMTs and Al_2O_3-based MOS-HEMTs, respectively. At V_{gs} = −40 V, the gate leakage current density of the TiO_2-based MOS-HEMTs is below 1 μA/mm and lower than the gate leakage current of both gate insulator materials Al_2O_3 and HfO_2 in both reverse and forward gate voltage regions. Besides, the gate leakage of the conventional HEMTs and MOS-HEMTs was reported by Liu *et al.* [8] using Al_2O_3 as gate dielectric, and the simulation

results were in good agreement with the experimental data. It is clear that the gate leakage current suppression in the MOS-HEMTs using TiO_2 as gate insulator is excellent. This indicates that the TiO_2 gate insulator is effective in increasing the breakdown voltage. A significant reduction in gate leakage current was observed for TiO_2 gate insulator.

Fig. 4 shows a comparison between the model output current characteristics obtained by using MATLAB calculation, Atlas-TCAD simulation, and experimental data [8] with different gate dielectrics such as Al_2O_3, HfO_2, and TiO_2 at V_{gs} = 0 V. The maximum drain saturation current I_{dssat} = 868.79 A/m for MOS-HEMTs device with TiO_2 as gate dielectric compared to both Al_2O_3 and HfO_2 is obtained, and the simulation results indicate good agreement with experimental data to confirm the analytical model. The same dimensions of GaN MOS-HEMTs with Al_2O_3 as gate insulator are exactly considered with the results obtained by Yagi *et al.* [13] using TiO_2 as gate insulator to reduce the gate leakage current. Improvements of 14% and 4.25% in I_{dssat} are obtained for MOS-HEMTs devices using TiO_2 than both Al_2O_3 and HfO_2, respectively.

-

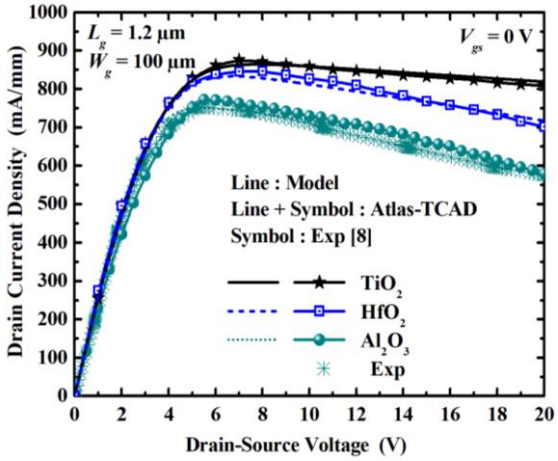

Fig. 4. Modeling of output current characteristics in comparison with Atlas-TCAD simulation results and the experimental data for three different devices.

Moreover, it is observed here that the drain saturation current decreases in GaN MOS-HEMTs by using low permittivity as gate insulator dielectric materials, following the same trend as reported by Yue *et al*. [10]. The AlGaN/AlN/GaN MOS-HEMTs with Al_2O_3 as gate insulator dielectric show a negative slope in the saturation region with V_{ds} changing from 5 V to 20 V due to the large negative differential conductance, which reduces electron mobility and performance in terms of power.

Besides, the self-heating effect (SHE) is the most important factor limiting the device's performance due to the reliability issue in high power operation conditions as well as the technique of thermal management, which has been taken into consideration in the simulation modeling of the drain current. However, the device in high power operation may output decreased drain current, which is mainly attributed to the negative differential conductance region at high current densities due to self-heating [43].

Furthermore, the self-heating-effect (SHE) is observed very clearly with Al_2O_3 as gate-dielectric based MOS-HEMTs and has also been considered in the analytical model to enable the reproduction of the device behavior for the full operating domain of voltages. Fig. 4 shows the effective incorporation of the SHE to obtain a close agreement between the simulated and measured output characteristics of the device by using Al_2O_3 as the gate dielectric. However, it is clear that in the range, the saturation current density of the curves considering the self-heating effect is smaller with TiO_2 as gate dielectric based MOS-HEMTs compared to both gate insulators (Al_2O_3 and HfO_2), due to the excellent thermal stability of TiO_2 at high power and high-temperature applications. The AlGaN/AlN/GaN MOS-HEMTs with TiO_2 as gate insulator dielectric

are promising candidates for high breakdown voltage and high switching speed device applications.

A comparison of the $I_{ds}(V_{gs})$ transfer characteristics of the proposed GaN-based MOS-HEMTs modeled and simulated with different gate dielectrics such as Al_2O_3, HfO_2, and TiO_2 at V_{ds} = 7 V is shown in Fig. 5. The device shows a maximum drain saturation current density of 1452 mA/mm at 2 V gate voltage by using a TiO_2 gate insulator, which is obtained by calibrating simulation results using the MATLAB program. Besides, it is obvious that the analytical model numerical results of the transfer characteristics are in good agreement with those extracted by Atlas-TCAD. The calibrated simulation results were compared with experimental data reported by Liu *et al*. [8] by using Al_2O_3 as the gate dielectric to validate the model calibration.

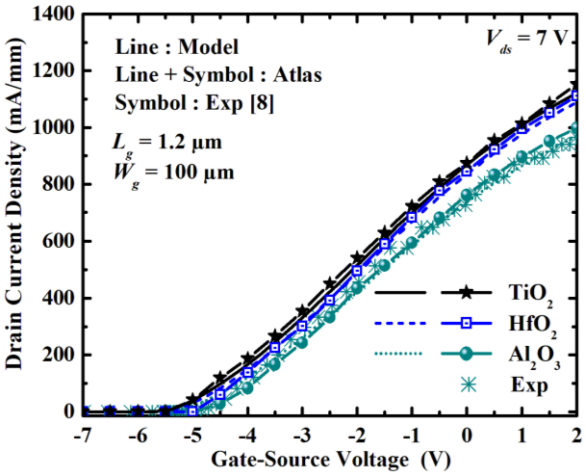

Fig. 5. $I_{ds} - V_{gs}$ characteristics of GaN MOS-HEMTs with different insulator dielectric materials Al_2O_3, HfO_2 and TiO_2 as gate dielectrics. Experimental data were extracted from [8].

Fig. 6 shows the comparison of the simulation and measured results of the transconductance with different gate dielectrics at V_{ds} = 7 V. The maximum transconductance ($g_{m,max}$) observed at V_{ds} = 7 V for the device with TiO_2 as gate dielectric is in good agreement with the physical model and the simulation results using Atlas-TCAD. It is also observed here that the transconductance decreases in GaN MOS-HEMTs using low permittivity gate insulator dielectric materials, as reported by Yue *et al*. [10] and Jena *et al.* [26]. Besides, improvements of 32.91% and 17.5% in $g_{m,max}$ are obtained for MOS-HEMTs device using TiO_2 over both Al_2O_3 and HfO_2, respectively. The large values of transconductance lead to high saturation velocity and higher carrier density n_s. On the other hand, higher transconductance in high-*k* gate dielectric materials suggests a linear improvement in the behavior of the MOS-HEMTs compared with the low-*k* gate dielectric GaN MOS-HEMTs, thus making them suitable for practical high power microwave applications.

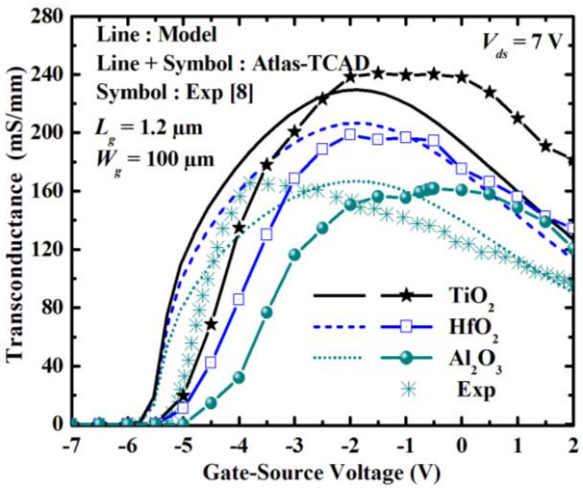

Fig. 6. Transconductance vs. gate voltage of GaN MOS-HEMTs device with Al_2O_3, HfO_2 and TiO_2 as gate dielectrics compared with experimental data, as reported in [8].

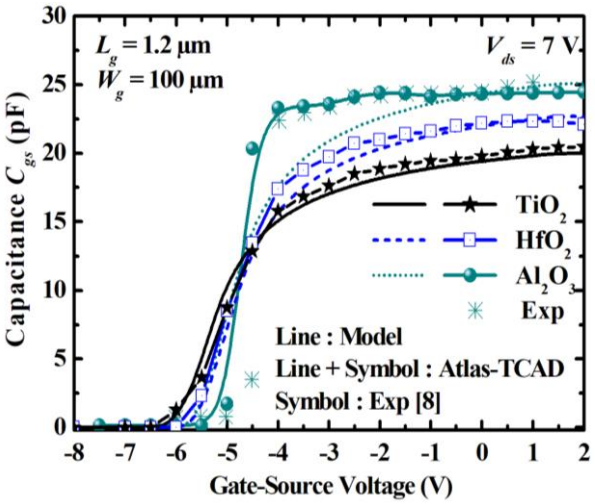

Fig. 7. Comparison of the capacitance C_{gs} with gate voltage of a device with Al_2O_3, HfO_2 and TiO_2 as gate dielectrics. Experimental data were extracted from [8].

Fig. 7 presents a plot of the gate-to-source capacitance (C_{gs}) versus gate-to-source voltage of GaN MOS-HEMTs with different gate dielectrics at V_{ds} = 7 V. The modeled simulation results of the capacitance C_{gs} have been obtained as compared with Atlas-TCAD and experimental data. In addition, it is obvious that the model-calibrated simulation results of the capacitance C_{gs} obtained by MATLAB are in good agreement with those extracted by Atlas-TCAD and experimental data, as reported in [8], concerning the Al_2O_3 gate dielectric as low-k. Besides, the device shows a lower gate-to-source capacitance C_{gs} of 22 pF at 0 V of gate-to-source bias voltage and $V_{ds} = 7$ V by using TiO_2 gate insulator material compared to the other insulators Al_2O_3 and HfO_2.

The variation of the gate-to-drain capacitance C_{gd} versus drain voltage modeled for GaN MOS-HEMTs with different gate dielectrics at V_{gs} = 0 V is shown in Fig. 8. The gate-to-drain capacitance decreases with an increase in the drain bias until it becomes zero in the saturation region for different gate insulator dielectric materials such as Al_2O_3, HfO_2, and TiO_2. This happens because of an increase in the drain-source bias voltage. Besides, it is seen here that the C_{gd} capacitance gradually varied function and then saturates. The MOS-HEMTs show a lower gate-to-drain capacitance C_{gd} of 8 pF at 1 V of drain bias voltage by using TiO_2 gate insulators compared with the other insulators Al_2O_3 and HfO_2. Thus, the use of TiO_2 high-κ as gate dielectric material could improve the frequencies (f_T and f_{max}) for dynamic (AC) electrical performance. Moreover, the modeled results of the gate-to-drain capacitance C_{gd} obtained by using MATLAB have been compared with simulation results extracted by Atlas-TCAD, there is good agreement between the physical model and the simulation results, which validates the capacitance modeling.

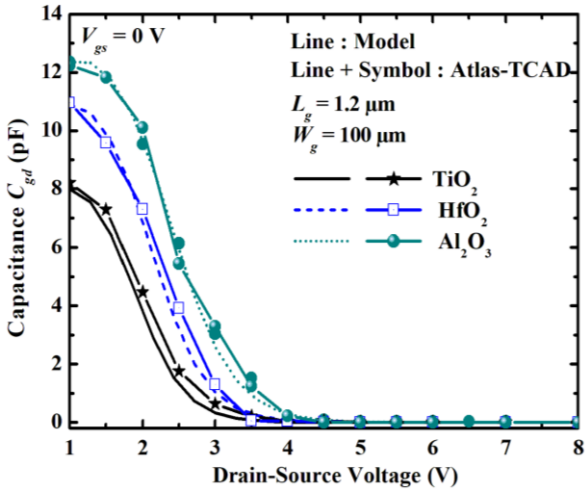

Fig. 8. Variation of C_{gd} capacitance with V_{ds} of a device with Al_2O_3, HfO_2 and TiO_2 as gate dielectrics at V_{gs} = 0 V.

The variations of the cut-off and the maximum oscillation frequencies with different gate insulator materials are shown in Fig. 9. The cut-off frequency starts initially to increase with gate-source voltage and decreases moderately as a result of the collective effect of the increase in the gate capacitance and the decreases in the transconductance, respectively.

Furthermore, it is clear from Fig. 9 by using TiO_2 as the gate insulator material for GaN MOS-HEMTs, the peak cut-off frequency shows an increase of 9% and 24.79% compared to HfO_2 and Al_2O_3, respectively. Besides, in the same Fig. 9 with TiO_2 for GaN MOS devices, the peak of maximum oscillation frequency f_{max} shows an increase of 13.04% and 33.64% over HfO_2 and Al_2O_3, respectively. Due to the high permittivity of the gate insulator dielectric material, which allows MOS-HEMTs to yield a large transconductance, subsequently increases frequencies (f_T and f_{max}) for the AC electrical performance reliability.

Moreover, the simulation results indicated by using TiO_2 as a gate insulator could improve the electrical performance of GaN HEMTs and could also promise candidature for the design of microwave integrated circuits and for high-power switching device applications.

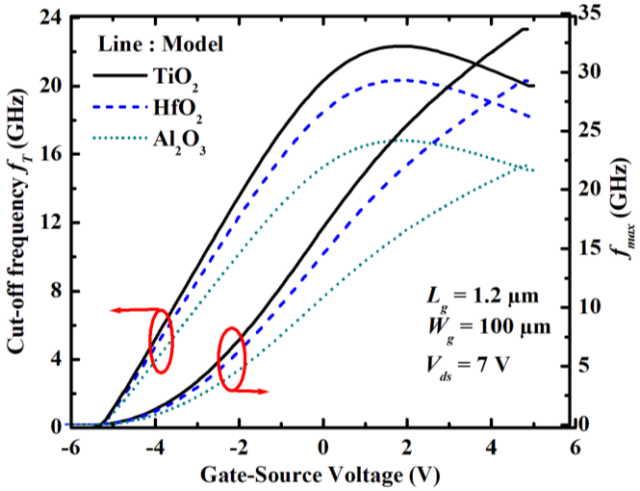

Fig. 9. Variation of the modeled frequencies (f_T and f_{max}) with gate voltage of AlGaN/GaN MOS-HEMTs device with different gate dielectrics at V_{ds} = 7 V.

4. CONCLUSION

The impact of the titanium dioxide (TiO_2) high-*k* gate insulator material on the DC and AC electrical performance of AlGaN/GaN MOS-HEMTs has been investigated. The parameter data introduced in the model were easily extracted from experiments were clearly linked to physical effects. Superior performance improvement in DC and AC electrical performance of GaN MOS-HEMTs using TiO_2 compared to both gate insulators Al_2O_3 and HfO_2 due to the high permittivity of TiO_2 and could translate to more efficient gate modulation. Besides, it is clear that the gate leakage current suppression in the MOS-HEMTs using TiO_2 as gate insulator is excellent. This indicates that the TiO_2 gate insulator is effective in increasing the breakdown voltage. Therefore, the presented simulation results suggest that the titanium dioxide (TiO_2) high-*k* gate insulator-based MOS-HEMTs could improve electrical reliability and also emerge as a potential candidate for high-power switching devices and high-temperature applications.

REFERENCES

[1] S. Verma, S.A. Loan and A.R.M. Alamoud. J. Comput. Electron. vol **17** (2018) pp. 256–264.
[2] L. Shen, S. Heikman, B. Moran, R. Coffie, N.Q. Zhang, D. Buttari, I.P. Smorchkova, S. Keller, S.P. DenBaars, and U.K. Mishra, IEEE Electron Device Lett. vol **22**, no 10 (2001) pp. 457–459.
[3] O. Ambacher, B. Foutz, J. Smart, J.R. Shealy, N.G. Weimann, K. Chu, M. Murphy, A..J. Sierakowski, W.J. Schaff, and L.F. Eastman, J. Appl. Phys. vol **87**, no 1 (2000) pp. 334–344.
[4] S. Verma, S.A. Loan and A.G. Alharbi. Superlattices Microstruct. vol **119**, (2018) pp. 181–193.
[5] S. Verma, S.A. Loan and A.R.M. Alamoud. IET Circuits, Devices and Systems, vol **12**, no 1 (2018) pp. 33–39.
[6] S. Mizuno, Y. Ohno, S. Kishimoto, K. Maezawa, and T. Mizutani, Jpn. J. Appl. Phys., Part 1. vol **41**, no 8 (2002) pp. 5125–5126.
[7] H. Yue, Y. Ling, M. Xiaohua, M. Jigang, C. Menyi, P. Caiyuan, W. Chong, and Z. Jincheng, IEEE Electron Device Lett. vol **32**, no 5 (2011) pp. 626–628.
[8] H.Y. Liu, C.S. Lee, W.C. Hsu, L.Y. Tseng, B.Y. Chou, C.S. Ho, and C.L. Wu, IEEE Trans. Electron Device. vol **60**, no 7 (2013) pp. 2231-2237.
[9] S.A. Loan, S. Verma, and A.R.M Alamoud. IET Electron. Lett, vol **52**, no 8 (2016) pp. 656 – 658.
[10] Y. Yue, Y. Hao, J. Zhang, J. Ni, W. Mao, Q. Feng, and L. Liu, IEEE Electron Device Lett. vol **29**, no 8 (2008) pp. 838–840.
[11] M.K. Lee and C.F. Yen, Electrochem. Solid-State Lett. vol **13**, no 10 (2010) pp. G87–G90.
[12] Y.S. Lin, C.C. Lu, and W.C. Hsu, Phys. Status Solidi C. vol **14**, no1-2 (2017) pp. 1–6.
[13] S. Yagi, M. Shimizu, M. Inada, Y. Yamamoto, G. Piao, H. Okumura, Y. Yano, N. Akutsu, H. Ohashi, Solid State Electron. vol **50**, no 6 (2006) pp. 1057–1061.
[14] S. Yagi, M. Shimizu, H. Okumura, H. Ohashi, Y. Yano, and N. Akutsu, Jpn. J. Appl. Phys. vol **46**, no 4B (2007) pp. 2309–2311.
[15] T.Y. Wu, S.K. Lin, P.W. Sze, J.J. Huang, W.C. Chien, C.C. Hu, M.J. Tsai, and Y.H. Wang, IEEE Trans. Electron Devices. vol **56**, no12 (2009) pp. 2911–2916.
[16] S.A. Campbell, H.S. Kim, D.C. Gilmer, B. He, T. Ma, and W.L. Gladfelter, IBM J Res Dev. vol **43**, no 3 (1999) pp. 383–392.
[17] I.P. Smorchkova, L. Chen, T. Mates, L. Shen, S. Heikman, B. Moran, S. Keller, S.P. DenBaars, J.S. Speck, and U.K. Mishra, J. Appl. Phys. vol **90**, no 10 (2001) pp. 5196–5201.
[18] T.C. Han, H.D. Zhao, L. Yang, and Y. Wang, Chin. Phys. B. vol **26**, no 10 (2017) pp. 107301–5.
[19] G. Amarnath, D.K. Panda, and T.R. Lenka, Int J Numer Modell Electron Networks Devices Fields. vol **32**, no 1 (2018) pp. 1–11.
[20] User Guide Manual, Atlas, Version 5.12.0.R./USA, Silvaco Inc, (2010).
[21] K. Jena, R. Swain, and T.R. Lenka, Int. J. Numer. Model. vol **30**, no 1, (2015).
[22] R. Swain, K. Jena, T.R. Lenka, Superlattices Microstruct. vol **84** (2015) pp. 54–65.
[23] S. Khandelwal, F. Tor A. In: Proceedings of the 2012 24th International Symposium on Power Semiconductor Devices and ICs, 3–7 June. (2012) – Bruges, Belgium. pp. 241–4.

[24] M. Lachab, M. Sultana, Q. Fareed, F. Husna, V. Adivarahan, and A. Khan, J. Phys. D: Appl. Phys. vol **47**, no 13 (2014) pp. 135108–14.
[25] M.F. Yigletu, S. Khandelwal, T.A. Fjeldly, and B. Iñiguez, IEEE Trans. Electron Devices. vol **60**, no 11 (2013) pp. 3746–3752.
[26] K. Jena, R. Swain, and T.R. Lenka, IET Circuits Devices Syst. vol **10**, no. 5 (2016) pp. 423–432.
[27] S. Verma S.A. Loan, M. Rafat, A. Rahman M. Alamoud, and S.A. Abbasi. J. Comput. Electron. vol **8**, no 3 (2019) pp. 941–950.
[28] Y.I. Jang, S.H. Lee, J.H. Seo, Y.J. Yoon, R.H. Kwon, M.S. Cho, B.G. Kim, G.M. Yoo, J.H. Lee, and I.M. Kang, J Semicond Tech Sci. vol **17**, no 2 (2017) pp. 223–229.
[29] S. Khandelwal, and T.A. Fjeldly, Solid-State Electron. vol **76**, (2012) pp. 60–66.
[30] G. Amarnath, R. Swain, and T.R. Lenka, Int J Numer Modell Electron Networks Devices Fields. vol **31**, no 1 (2017) pp. 1–8.
[31] M. Gonschorek, J.F. Carlin, E. Feltin, M.A. Py, and N. Grandjean, Int J Microw Wirel Technol. vol **2**, no 1 (2010) pp. 13-20.
[32] H. Chandrasekar S. Kumar, K.L. Ganapathi, S. Prabhu, S.B. Dolmanan, S. Tripathy, S. Raghavan, K. N. Bhat, S. Mohan, R. Muralidharan, N. Bhat, and D.N. Nath, IEEE Trans. Electron Devices. vol **65**, no 9 (2018) pp. 3711–3718.
[33] A. Bouazra, S. Abdi-Ben Nasrallah, M. Said, and A. Poncet. Res. Lett. Phys. vol **2008**, (2008) pp. 1–5.
[34] S. Monaghan, P.K. Hurley, K. Cherkaoui, M.A. Negara, A. Schenk., Solid. State. Electron. vol **53**, no 4 (2009) pp. 438–444.
[35] S. Clima, B. Kaczer, B. Govoreanu, M. Popovici, J. Swerts, A.S. Verhulst, M. Jurczak, S.D. Gendt, and G. Pourtois, IEEE Electron Device Lett. vol **34**, no 3 (2013) pp. 402–404.
[36] X. Qin, L. Cheng, S. McDonnell, A. Azcatl, H. Zhu, J. Kim, R.M. Wallac, J Mater Sci: Mater Electron. vol **107**, no 8 (2015) pp. 081608–081612.
[37] P.J. Hansen, V. Vaithyanathan, Y. Wu, T. Mates, S. Heikman, U.K. Mishra, R.A. York, D.G. Schlom, and J.S. Speck, J Vac. Sci. Technol. B. vol **23**, no 2 (2005) pp. 499–506.
[38] V. Tokranov, S.L. Rumyantsev, M.S. Shur, R. Gaska, S. Oktyabrsky, R. Jain, and N. Pala, Phys. Stat. Sol. vol **1**, no 5 (2007) pp. 199–201.
[39] T. Kubo and T. Egawa, Phys. B: Condens. Matter. vol **571**, no 15 (2019) pp. 210–212.
[40] T. Kubo, M. Miyoshi, and T. Egawa, "Analysis of Post-Deposition Annealing Effects on Insulator/Semiconductor Interface of Al_2O_3/AlGaN/GaN High-Electron-Mobility Transistors on Si Substrates," International Conference on Solid State Devices and Materials, Sapporo, Japan, (2015) pp. 192–193.
[41] Z. Gao, M.F. Romero, and F. Calle, IEEE Trans. Electron Devices. vol **65**, no 8 (2018) pp. 3142–3148.
[42] S. Dargahi, and Sheldon S. Williamson, "On the Suitability of Gallium-Nitride (GaN) Based Automotive Power Electronics," IEEE Vehicle Power and Propulsion Conference, 1938 (2010) pp. 1–3.
[43] Q. Hu, B. Hu, C. Gu, T. Li, S. Li, S. Li, X. Li, and Y. Wu, IEEE Trans. Electron Devices., vol. **66**, no 11, (2019) pp. 4591– 4596.